



# Crust and upper mantle of the western Mediterranean – Constraints from full-waveform inversion

Andreas Fichtner<sup>a,\*</sup>, Antonio Villaseñor<sup>b</sup>

<sup>a</sup> Department of Earth Sciences, ETH Zurich, Zurich, Switzerland

<sup>b</sup> Institute of Earth Sciences Jaume Almera, ICTJA-CSIC, Barcelona, Spain



## ARTICLE INFO

### Article history:

Received 21 April 2015

Received in revised form 13 July 2015

Accepted 16 July 2015

Available online xxxx

Editor: B. Buffett

### Keywords:

seismic tomography

western Mediterranean

full-waveform inversion

computational seismology

## ABSTRACT

We present a full-waveform tomographic model of the western Mediterranean crust and mantle constructed from complete three-component recordings from permanent and temporary networks. The incorporation of body and multi-mode surface waves in the period range from 12–150 s allows us to jointly resolve crustal and mantle structures, including the Guadalquivir, Tajo and Ebro basins at shallow depth, as well as the western Mediterranean subduction system in the transition zone. No mantle plumes can be detected beneath the European Cenozoic rift system, including the Massif Central. In addition to the well-studied Alboran slab, a strong E-W trending high-velocity anomaly is present around 200–300 km depth beneath the Algerian coast. This previously undetected African slab is detached from the surface and broken into two segments. It may be interpreted as the slab that caused the opening of the Liguro-Provençal basin through successive roll-back between 35–15 Ma.

© 2015 Elsevier B.V. All rights reserved.

## 1. Introduction

### 1.1. The western Mediterranean

The Cenozoic evolution of the Mediterranean region (Fig. 1) is marked by the subduction of oceanic lithosphere and associated processes. While the geodynamics of the central and eastern Mediterranean for the past ~35 Ma is well understood (e.g. Faccenna et al., 2014), the development of the western Mediterranean remains debated. Estimates for the westward extension of the Alboran region, for instance, range from ~250 km (Platt et al., 2003; Faccenna et al., 2004), over 400 km (Spakman and Wortel, 2004) to 500–900 km (Loneragan and White, 1997). Proposed physical mechanisms for the extension and formation of the Betic-Rif orogenic system include extensional collapse (Dewey, 1988; Platt et al., 2003; Molnar and Houseman, 2004), lithospheric delamination or slab-rollback (Loneragan and White, 1997; Faccenna et al., 2004; Spakman and Wortel, 2004), and a change in subduction direction (Vergés and Fernández, 2012). Further east of the Alboran region, beneath the Algerian coast, the existence of northward subduction has been proposed by evolution models (e.g. Faccenna et al., 2014). However, no deep seismicity or island arc is present, and existing tomographic models of the region have not

convincingly imaged structures that could be associated with subducted lithosphere.

Key to an improved quantitative understanding of the western Mediterranean are tomographic models of the crust and mantle. Early regional models that include the Mediterranean were derived by Nolet (1977) and Cara et al. (1980) from the analysis of Rayleigh wave dispersion at few long-period stations in Europe. More recently, numerous tomographic models of the Mediterranean region have been constructed using surface waves (e.g. Villaseñor et al., 2001; Palomeras et al., 2014), body wave traveltimes (e.g. Spakman et al., 1993; Villaseñor et al., 2003; Piromallo and Morelli, 2003; Koulakov et al., 2009; Bezada et al., 2013; Bonnin et al., 2014), or a combination of both (e.g. Chang et al., 2010; Fichtner et al., 2013b; Zhu et al., 2015). However, most of these models have insufficient resolution in the western Mediterranean and northern Africa, either due to a lack of data or as a result of methodological restrictions. The latter include the restriction to either surface- or body-wave data that by themselves have limited resolution, and the need for crustal corrections that prevent the use of shorter-period ( $\lesssim 20$  s) surface waves required for the resolution of shallow structure.

Here we use the opportunity provided by recent dense deployments of broadband stations (Fig. 2) in the region to obtain a new model of the western Mediterranean crust and mantle, using full-waveform inversion of three-component recordings in the period range 12–120 s.

\* Corresponding author.

E-mail address: andreas.fichtner@erdw.ethz.ch (A. Fichtner).

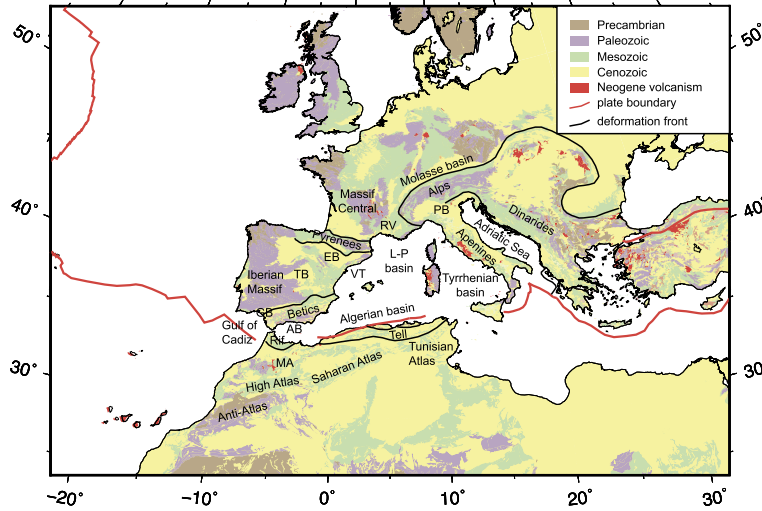


**Fig. 1.** Geologic map of the Mediterranean and surrounding regions. Selected features referred to in the text are labelled. Key to abbreviations: AB: Alboran basin, EB: Ebro basin, GB: Guadalquivir basin, L-P basin: Liguro-Provençal basin, MA: Middle Atlas, PB: Po basin, RV: Rhône valley, TB: Tajo basin, VT: Valencia trough.

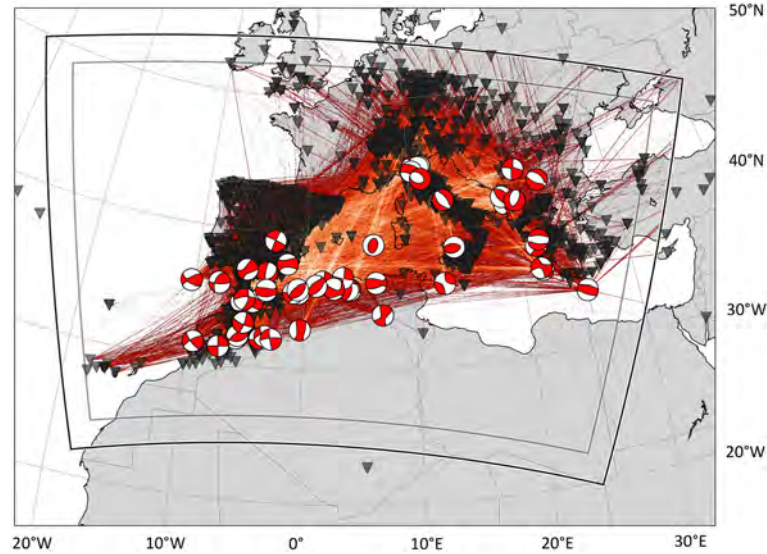


**Fig. 2.** Source-receiver distribution in the western Mediterranean region. Beachballs indicate the source mechanisms and locations of the 52 earthquakes used in our inversion. Great circles connecting sources and receivers are plotted in lighter colour when coverage is high. The black solid box marks the boundary of the computational domain for numerical wave propagation. Recordings are only chosen from within the inner grey box to avoid contamination by artificial reflections from imperfect absorbing boundaries.

### 1.2. Full-waveform inversion

Following early developments in the 1980s (e.g. Lailly, 1983; Tarantola, 1984), full-waveform inversion has only recently developed into a viable tool for the assimilation of seismic waveform data into 3-D Earth models (e.g. Chen et al., 2007; Tape et al., 2010; Rickers et al., 2013). Using complete seismograms instead of few selected phases generally improves tomographic resolution. The crust and upper mantle benefit most from the application of full-waveform inversion for various reasons: (i) The numerical forward modelling produces accurate synthetic seismograms in the presence of strong heterogeneities. This aspect is particularly important for short-period surface waves propagating near sharp ocean–continent boundaries. (ii) Complex 3-D Earth structure results in complex 3-D sensitivity kernels that can be computed accurately with the help of adjoint techniques. The use of more approximate sensitivity kernels, based for instance on ray theory, may reduce or impede convergence in the iterative nonlinear inversion. (iii) The inversion of complete waveforms, including body and surface waves, constrains both crustal and mantle

structure, without requiring crustal corrections. Furthermore, the vertical smearing in pure body wave tomography is reduced, thus avoiding the appearance of artificial plume-like features.

### 1.3. Objectives and outline

The objective of this work is to exploit both the high station density in the western Mediterranean and the benefits of full-waveform inversion that naturally assimilates all seismic wave types into a 3-D model where crust and mantle are jointly constrained. We deliberately stay on a rather technical level, emphasising quantitative aspects of the model. A detailed geologic interpretation is beyond the scope of this paper but work in progress.

This paper is organised as follows: We begin in Section 2 with a description of the waveform data used in the inversion. This includes information on provenance, selection, and processing. Section 3 summarises the construction of the tomographic model, providing details on the initial model, forward modelling and nonlinear iterative inversion. A key element of this work is a quantitative resolution analysis presented in Section 4. This will be

followed by a description of the model, including crustal structure, anisotropy and upper-mantle heterogeneities. In Section 7 we provide a more detailed discussion of selected structural features, as well as a comparison with previous tomographic models.

## 2. Data

The data used in this study are a compilation of three-component seismograms from earthquakes that occurred in the Mediterranean region (Fig. 2). For broadband stations belonging to permanent networks we obtained waveform data from IRIS ([www.iris.edu](http://www.iris.edu)) and the Virtual European Broadband Seismic Network (VEBSN) of ORFEUS ([www.orfeus-eu.org](http://www.orfeus-eu.org)). We complemented this dataset with data from regional networks, and with data from temporary broadband deployments. The largest of these is IberArray (Díaz et al., 2009) that covered northern Morocco and the Iberian Peninsula in three consecutive deployments, starting in the south in 2007 and ending in the north in 2013, resulting in a total of 167 sites. Subsequently, other temporary networks have been installed in Spain and Morocco, expanding and densifying the coverage of IberArray. The PASSCAL experiment PICASSO (90 stations in southern Spain and northern Morocco) and smaller arrays deployed by the Universities of Münster, Germany (15 stations) and Bristol, UK (6 stations) have greatly improved the coverage in previously unsampled regions of central and southern Morocco.

For events with magnitudes above 5.0, we obtained initial moment tensor estimates from the Global Centroid Moment Tensor catalog ([www.globalcmt.org](http://www.globalcmt.org)). To optimise coverage, we incorporated data from smaller earthquakes with magnitudes between 3.6 and 4.0 that occurred during the operation period of the temporary broadband networks (2007–2013). For these earthquakes, we obtained initial moment tensor solutions using the method of Herrmann et al. (2011).

To prepare the data for the inversion, we removed instrument responses and bandpass filtered between 12 and 120 s period. We then inspected all recordings and rejected those where the signal-to-noise ratio was below  $\sim 10$ . Our final dataset contains 13,089 three-component recordings from 52 events. The source-receiver distribution is shown in Fig. 2.

## 3. Model construction

Our model constitutes a regional refinement of the Eurasian model by Fichtner et al. (2013b). For the regional refinement in the western Mediterranean we apply full-waveform inversion based on spectral-element solutions of the anisotropic, viscoelastic wave equation. Our GPU-accelerated solver operates in the natural spherical coordinate system (Gokhberg and Fichtner, *in press*) and applies perfectly-matched layers to absorb unphysical reflections from the boundaries of the computational domain. To ensure sufficient accuracy of the numerical solutions, we employ 2 elements per minimum wavelength.

For the comparison between observed and synthetic seismograms we employ our recently developed *Large-scale Seismic Inversion Framework* (LASIF, Krischer et al., 2015). In addition to data management and processing, LASIF provides a pre-selection of time windows where observed and synthetic waveforms are sufficiently similar to allow for meaningful measurements of time- and frequency-dependent phase differences (Fichtner et al., 2008). Subsequently, we manually inspect the data and refine the window selection. Windows comprise any type of seismic wave, including body waves, fundamental- and higher-mode surface waves, as well as unidentified phases. The window selection procedure is repeated on average every 5 iterations to ensure that information from as many windows as possible is exploited.

Following the measurements, LASIF computes adjoint sources, needed as input in the adjoint calculations that produce sensitivity kernels (e.g. Tarantola, 1984; Tromp et al., 2005; Fichtner et al., 2006). The sensitivity kernels are used to drive a conjugate-gradient optimisation. During the inversion no distinction is made between crustal and mantle structure. Specifically, the effective crustal thickness and crustal velocities are free to vary as demanded by the data. In addition to eliminating the need for crustal corrections, this approach ensures that artefacts from incorrect shallow structure are minimised. In contrast to the approach advocated by Fichtner et al. (2013a), we did not use updated western Mediterranean structure to improve the surrounding Earth model. This type of multiscale refinement is work in progress and will be reported in later publications.

We terminated the optimisation after 20 iterations, that is when the misfit reduction in one iteration dropped below 1%. After iterations 5 and 15 we re-inverted for the source locations and origin times. Inversions for the moment tensor components did not lead to any significant misfit reduction after iteration 5, and were thus not attempted again. The total misfit reduction after 20 iterations was nearly 80%.

## 4. Resolution analysis

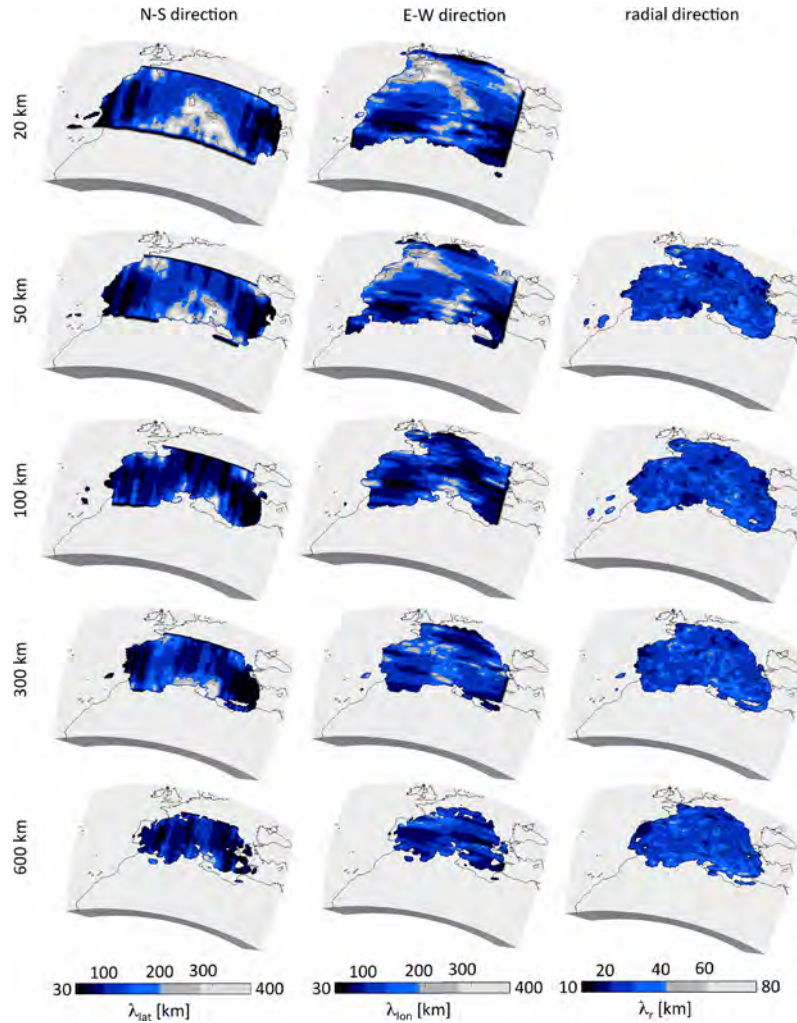
Before the detailed presentation of the final model in Sections 5 and 6, we provide a resolution analysis that will later serve as interpretative aid. We quantify resolution in terms of direction- and position-dependent resolution length, defined as the width of the point-spread function in a given location and direction (e.g. Backus and Gilbert, 1968; Yanovskaya, 1997). Since point-spread functions in the vicinity of the optimal model are equal to the columns of the Hessian, we can use second-order adjoints (Fichtner and Trampert, 2011) to extract resolution information. To keep computational requirements low, we employ random probing techniques that estimate resolution length from the application of the Hessian to a small number (typically  $<5$ ) of random test models (Fichtner and van Leeuwen, 2015). Our resolution analysis is more quantitative and less computationally expensive than recovery tests of the checkerboard-type that may be misleading even if the Earth were a checkerboard, too (Lévesque et al., 1993).

Fig. 3 summarises the 3-D distributions of resolution length in N-S, E-W and radial directions. As already observed in ray tomography, resolution length is strongly heterogeneous and anisotropic (e.g. Yanovskaya, 1997). In the horizontal directions, resolution length within the upper 50 km varies from 30–400 km. While local minima at shallow depth appear beneath the Aegean and the Iberian Peninsula where coverage is dense, resolution is less optimal beneath the south-central Mediterranean where few surface ray paths cross.

With increasing depth, resolution length characteristics are less dominated by surface waves, and more a function of body wave coverage. Therefore, the resolved volume shrinks with increasing depth. Nevertheless, resolution lengths on the order of 50 km are possible to depths of  $\sim 600$  km in regions where sufficiently many wave paths cross. As a result of predominantly E-W oriented source-receiver paths (Fig. 2), resolution in N-S direction is mostly better than in E-W direction.

Resolution length in radial direction is more homogeneous and shorter than in the horizontal directions because fundamental- and higher-mode surface waves enter the inversion. Regions with poor horizontal resolution may in fact be well resolved in radial direction when few surface wave paths spread heterogeneities over wide areas while still constraining them to the correct depth range. Resolution in radial direction could not be computed at 20 km depth because a reliable estimate of the point-spread function width requires a sufficiently large volume around the location of





**Fig. 3.** Resolution length in N-S direction (left), E-W direction (centre) and radial direction (right). Regions where the volume of the local point-spread functions is below 1% of the maximum point-spread function volume, are blanked.

interest that is not available close to the surface (Fichtner and van Leeuwen, 2015). A detailed resolution analysis of the surrounding model can be found in Fichtner et al. (2013b).

## 5. Crustal and uppermost-mantle structure

The upper 300 km of the Earth are marked by rapid transitions from crust to mantle, and from oceanic to continental domains. Since these strong variations complicate the definition of a meaningful 1-D reference model, we present 3-D distributions of *absolute* velocities. As reference frequency we choose 1 Hz. The attenuation model is a version of QL6 (Durek and Ekström, 1996) where the upper 300 km have been replaced by a cubic spline to avoid artificial phase velocity discontinuities when converting to different frequencies.

To visualise crustal and mantle structure in Figs. 4 and 5, we employ a non-conventional colour scale. Crustal S velocities roughly ranging from <2.5–4.0 km/s are represented in greyscale. Colours from red to blue are used for upper-mantle velocities of 4.0–5.0 km/s and above. The transition from crust to mantle thus appears as a change from greyscale to colour. The visualisation of absolute velocities emphasises structural features that are more difficult to identify in images of velocity variations relative to a horizontal average. These include lateral changes in crustal depth, and the presence and extent of a low-velocity zone.

### 5.1. Absolute isotropic S velocity

We define the absolute isotropic S velocity as  $v_S^2 = \frac{2}{3}v_{SV}^2 + \frac{1}{3}v_{SH}^2$ . Horizontal slices through the upper 40 km are shown in Fig. 4. Vertical slices from the surface to 300 km can be seen in Fig. 5.

Around 5 km depth, lateral variations in crustal velocity are on the order of 25%. The highest velocities around 3.8 km/s can be found beneath the Iberian Massif and the Massif Central. Sedimentary basins, including the Guadalquivir, Tajo, Ebro, Po and Molasse basins, as well as the Rhône valley account for the lowest velocities of 2.7 km/s and below.

Regional differences in crustal thickness are most visible in the 25 km slice in Fig. 4. While the western Mediterranean basin at 25 km depth already reveals elevated mantle velocities of up to 4.7 km/s, south-western Iberia is still dominated by crustal velocities as low as 3.5 km/s. The 40 km depth slice in Fig. 5 shows that the thickest crust can be found beneath the western Betics, the Pyrenees, the Apennines, the Dinarides, and in the Alps (Fig. 1).

The vertical slices in Fig. 5 reveal the presence of a pronounced high-velocity lid extending from the Moho to mostly less than 100 km depth. Locally,  $v_S$  within the upper 100 km reaches values of up to 5.0 km/s, that is  $\sim 10\%$  faster than the global averages of most radially symmetric Earth models in the uppermost mantle (e.g. Dziewoński and Anderson, 1981; Kennett and Engdahl, 1991). No obvious correlation exists between the thickness of this lid and the thickness of the overlying crust.

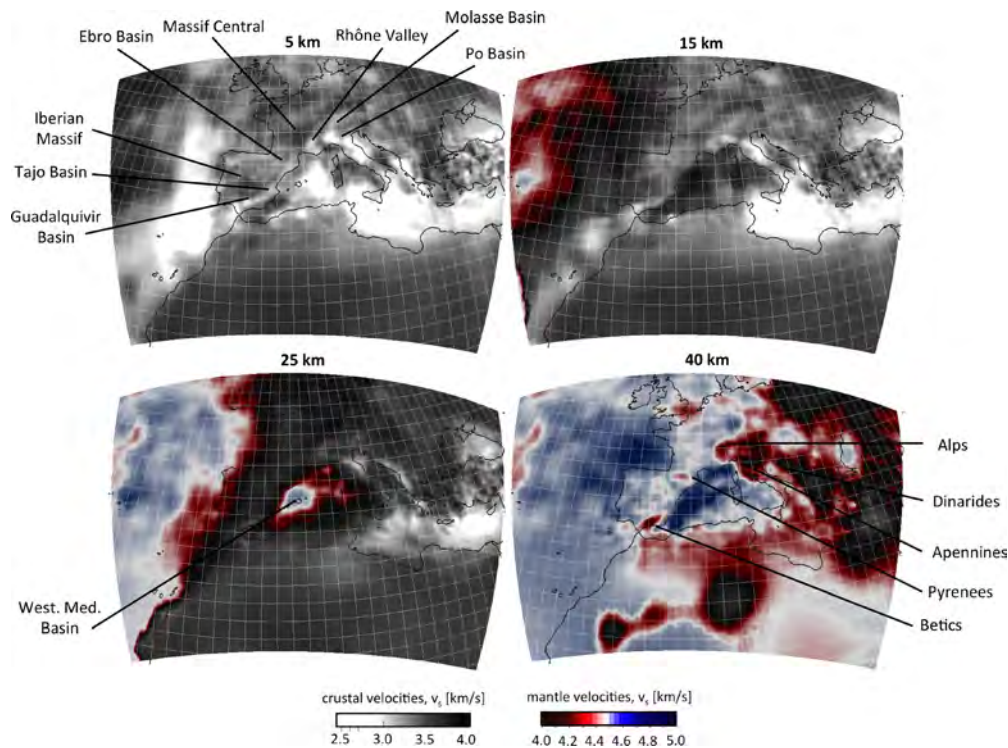


**Fig. 4.** Horizontal slices through the absolute isotropic S velocity ( $v_s$ ) distribution at shallow depths of 5–40 km and at the reference frequency of 1 Hz. Greyscale roughly corresponds to crustal velocities of <2.5 to 4.0 km/s, and colours from dark red over white to dark blue represent mantle velocities of 4.0 to >5.0 km/s. Structural features mentioned in the text are labelled. (For interpretation of the references to colour in this figure legend, the reader is referred to the web version of this article.)

A broad low-velocity zone can be found at depths ranging on average from 80 to 250 km depth, with local interruptions only in the vicinity of the Alboran and African slabs, to be discussed later in Sections 6 and 7. Around 100 km depth beneath the eastern Alboran Sea,  $v_s$  nearly drops to 4.0 km/s; a value more typical for the lower crust. The transition between the high-velocity lid and the low-velocity zone is locally sharp to within the vertical resolution length, that is from  $\sim 4.8$  to  $\sim 4.1$  km/s (–16%) over 20 km depth.

## 5.2. Radial anisotropy

In our inversion, we allow for radial anisotropy, i.e. anisotropy with hexagonal symmetry about the radial axis. Fig. 6 summarises the 3-D distribution of S wave anisotropy in terms of the difference between  $v_{SH}$  and  $v_{SV}$ , normalised by the isotropic S velocity  $v_s$ .

In the upper 50 km, strong positive ( $v_{SH} > v_{SV}$ ) anisotropy of up to 25% is required in the continental regions, mostly by surface waves with periods below  $\sim 20$  s. Isolated patches of negative radial anisotropy ( $v_{SH} < v_{SV}$ ) exist near the hypocentres of some earthquakes, and may thus be artefacts related to event mislocation or near-field effects.

Around 70 km depth, more extended regions of negative anisotropy appear, and the amplitude of anisotropy drops to less than 10%. Below 100 km depth, the strength of anisotropy is reduced to a few percent. The rapid drop of anisotropy strength near 100 km depth is clearly visible in the radially averaged S velocities shown in Fig. 7; in comparison to the Preliminary Reference Earth Model (PREM, Dziewoński and Anderson, 1981). While radial anisotropy in PREM is present to depths of 220 km, the regionally averaged radial anisotropy beneath the western Mediterranean is nearly absent below 100 km.

While differences in anisotropy between PREM and our model may to some extent result from the different averaging processes, the largest contribution certainly comes from the incorporation of

crustal anisotropy that was forced to be absent in PREM. Strong crustal anisotropy in our model is required by surface waves with periods below  $\sim 20$  s that were not part of the long-period ( $>60$  s) data set used in the construction of PREM. Since long-period surface waves are unable to resolve crustal structure, they can trade the absence of anisotropy in the crust against anisotropy at greater depth. This ambiguity between fine-scale (shallow) structure and large-scale anisotropy is well-understood (e.g. Ferreira et al., 2010) and may only be reduced by the incorporation of shorter-period data, as done in our inversion. In a different context, Bolt (1991) noted that the anisotropy in PREM may be the artefact of a non-existing average crustal structure that represents neither oceanic nor continental crust.

Strong lithospheric anisotropy is demanded by the data, but its origin remains ambiguous. Possible contributions to the perceived anisotropy include (i) intrinsic anisotropy from the large-scale coherent alignment of anisotropic minerals, (ii) differential resolution of  $v_{SH}$  and  $v_{SV}$  heterogeneities, and (iii) inherent trade-offs between unresolved small-scale structure and large-scale anisotropy (e.g. Backus, 1962; Capdeville et al., 2010; Fichtner et al., 2012). Since a quantitative separation of these contributions is currently impossible, we abstain from an interpretation of the anisotropy in our model in terms of geodynamic processes.

## 6. Mantle structure

Since the presence of seismic discontinuities near 410 and 660 km depth renders the visualisation of absolute velocities difficult, we present mantle structure relative to the regional lateral average shown in Fig. 7. The regional average differs from PREM (Dziewoński and Anderson, 1981) mostly in the absence of the 220 km discontinuity that our data do not require. Within the upper 200 km of the mantle, variations in  $v_s$  range between –12.2% and 13.1%, meaning that heterogeneities are stronger than in most other S velocity models where  $v_s$  varies by less than 10% in the

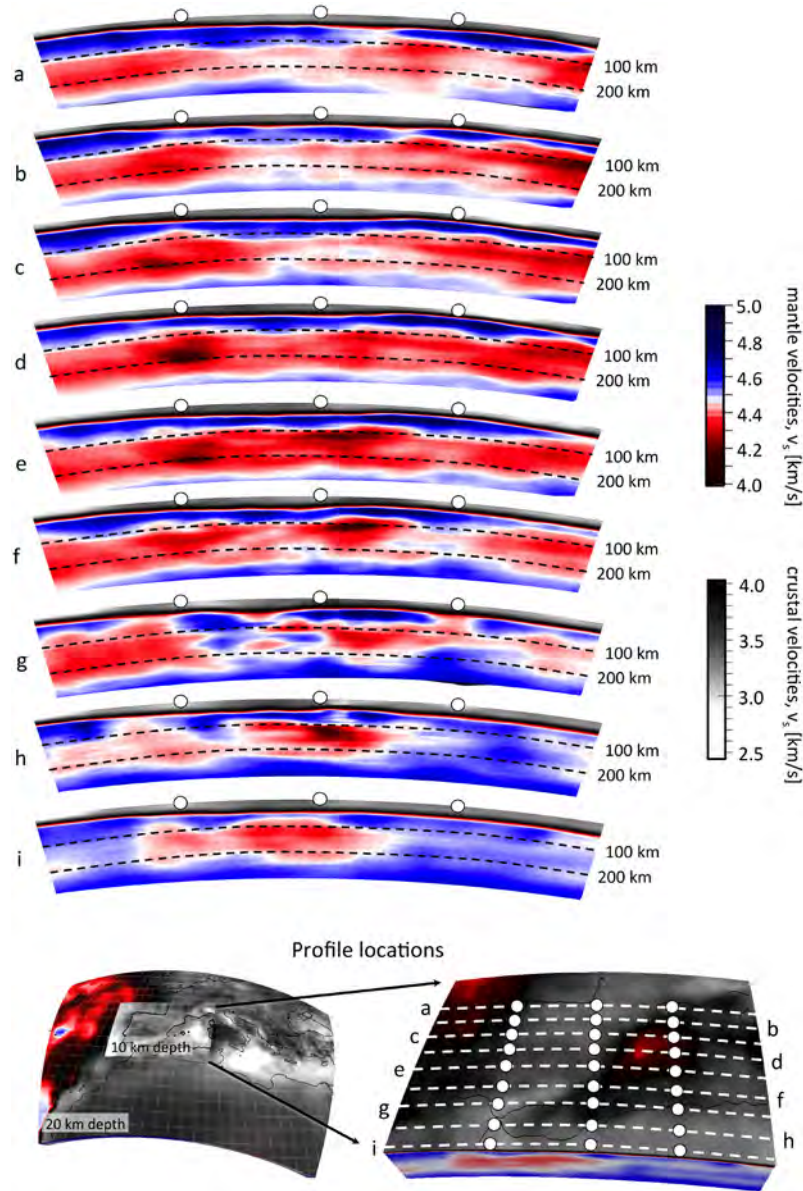


**Fig. 5.** Vertical profiles through the absolute isotropic S velocity  $v_s$  at the reference frequency of 1 Hz. The locations of the profiles are shown by the white-dotted lines in Fig. 4. The positions of the white dots and the colour scale are the same as in Fig. 4. (For interpretation of the references to colour in this figure legend, the reader is referred to the web version of this article.)

same depth range (e.g. Villaseñor et al., 2001; Chang et al., 2010). The increased strength of heterogeneities is most likely the result of increased resolution, i.e. less spatial smearing. Vertical and horizontal slices through the  $v_s$  heterogeneities are shown in Figs. 8 and 9.

Pronounced low-velocity anomalies appear beneath the Liguro-Provençal basin, the Massif Central, and the Olot volcanic field; but also beneath southern and western Iberia where recent volcanism is absent. All of these anomalies are confined to the upper 150–200 km of the mantle. At depths below  $\sim 150$  km, mantle structure is dominated by the high-velocity anomalies of the Mediterranean subduction system. The eastward dipping Adria-Dinaride slab and the westward dipping Calabria slab are well-defined and clearly visible in cross-section DD' of Fig. 8. The Alboran slab, as well as various pronounced E-W trending high-velocity segments beneath the Algerian coast appear in cross-sections aa' to dd'. These features, interpreted as the African slab, are discussed in more detail in Section 7.1.2.

## 7. Discussion

In the following paragraphs, we provide a discussion of specific structural features in our model, as well as a qualitative comparison with previously published results.

### 7.1. Specific structural features

#### 7.1.1. The European Cenozoic Rift System

The most prominent features in the uppermost mantle – shown in Figs. 8 and 9 – are localised low-velocity anomalies approximately following the European Cenozoic Rift System (ECRS). A continuous corridor of low velocities extends from the Massif Central into northern Africa, with pronounced velocity minima beneath centres of tectonic and volcanic activity. These include the Massif Central, the Catalan Volcanic Zone, and the Valencia Trough. The low-velocity anomaly associated with the Valencia Trough is not directly centred on it, but to the SW, extending beneath the



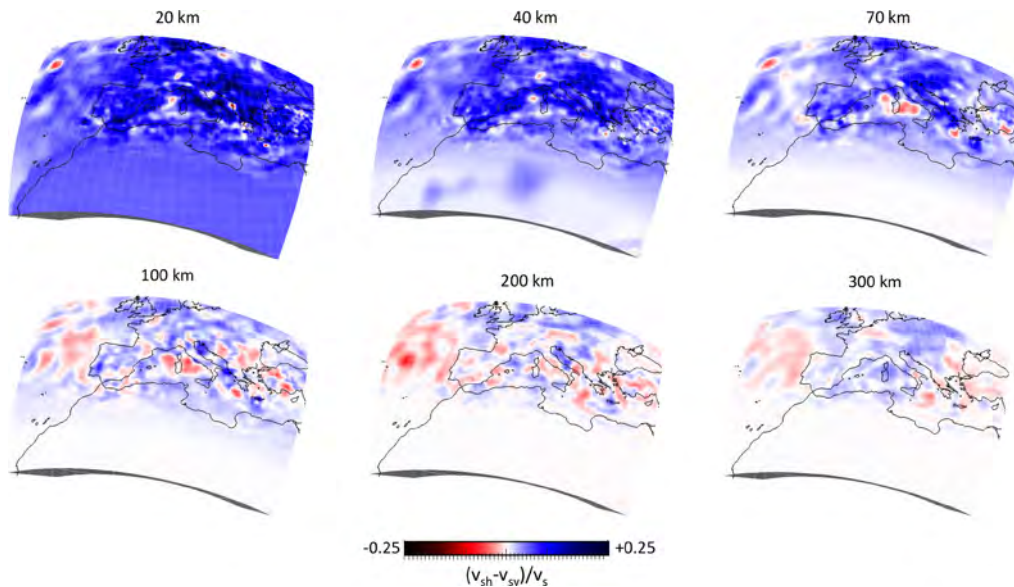


**Fig. 6.** Horizontal slices through the distribution of relative radial anisotropy,  $(v_{SH} - v_{SV})/v_S$ , at depths ranging from 20–300 km. Below 300 km depth, radial anisotropy is negligible.

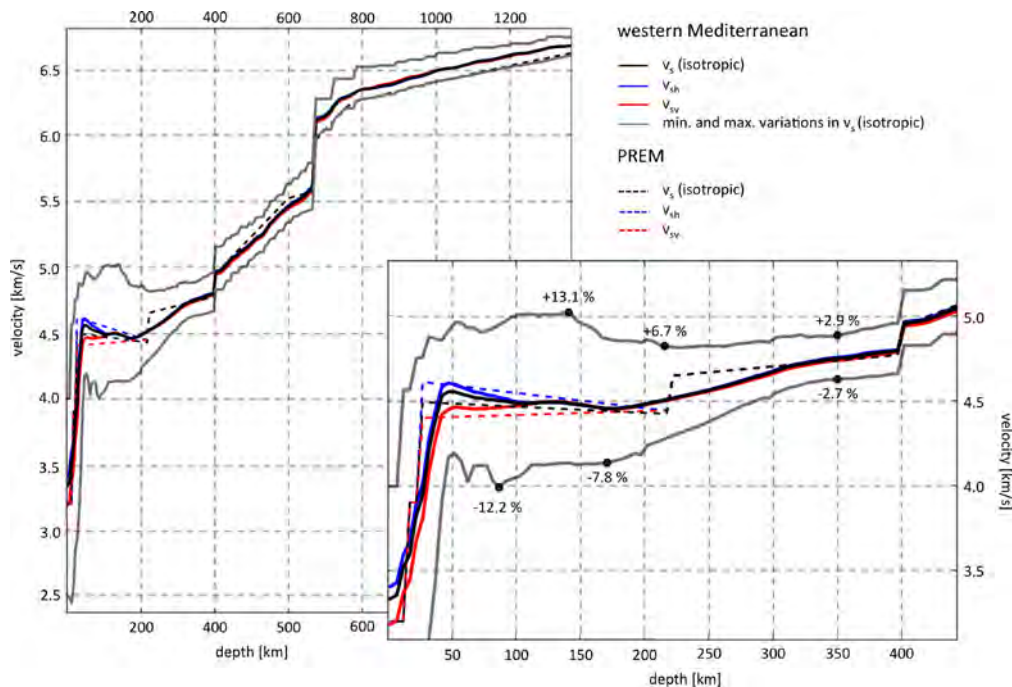


**Fig. 7.** Radially averaged S velocity structure in comparison to the Preliminary Reference Earth Model (PREM, Dziewoński and Anderson, 1981). The solid black, blue and red lines represent the radially averaged isotropic S velocity  $v_s$ , SH velocity  $v_{SH}$ , and SV velocity  $v_{SV}$ , respectively. Grey lines indicate the minimum and maximum  $v_s$  at a given depth. Velocities for PREM are plotted as dashed lines in the same colours. To ensure comparability, the reference frequency for all velocities is 1 Hz. A selection of percentage variations is shown in the upper-mantle inset to the left. The highest velocity perturbations appear within the Hellenic slab, and the lowest ones beneath the Valencia trough and the Massif Central. (For interpretation of the references to colour in this figure legend, the reader is referred to the web version of this article.)

eastern Betics. Furthermore, the ECRS is well imaged in northern Europe where distinct anomalies appear beneath the Bohemian Massif, and the upper and lower Rhine Graben. Strong negative anomalies reaching  $-12\%$  are generally confined to the upper 200 km.

Mantle plumes with vertically elongated tails and laterally spreading plume heads have been repeatedly proposed to be the source of volcanism along the ECRS (e.g. Granet et al., 1995; Goes et al., 1999; Ritter et al., 2001). Such plumes, however, are not present in our model. The resolution analysis presented in Section 4 implies that the diameter of a mantle plume between

300–600 km depth would have to be less than  $\sim 100$  km in order to remain seismically invisible. Vertically stretched anomalies are a common feature of teleseismic traveltimes tomography that may result from insufficient coverage in the upper mantle where all incoming body waves travel nearly vertically. The addition of surface wave data can reduce the vertical smearing, thereby localising apparently deep-reaching anomalies to shallower depths. Since the natural combination of body and surface waves in full-waveform inversion does not reveal any mantle plume beneath central and western Europe, a deep-mantle source of volcanism along the ECRS seems unlikely.

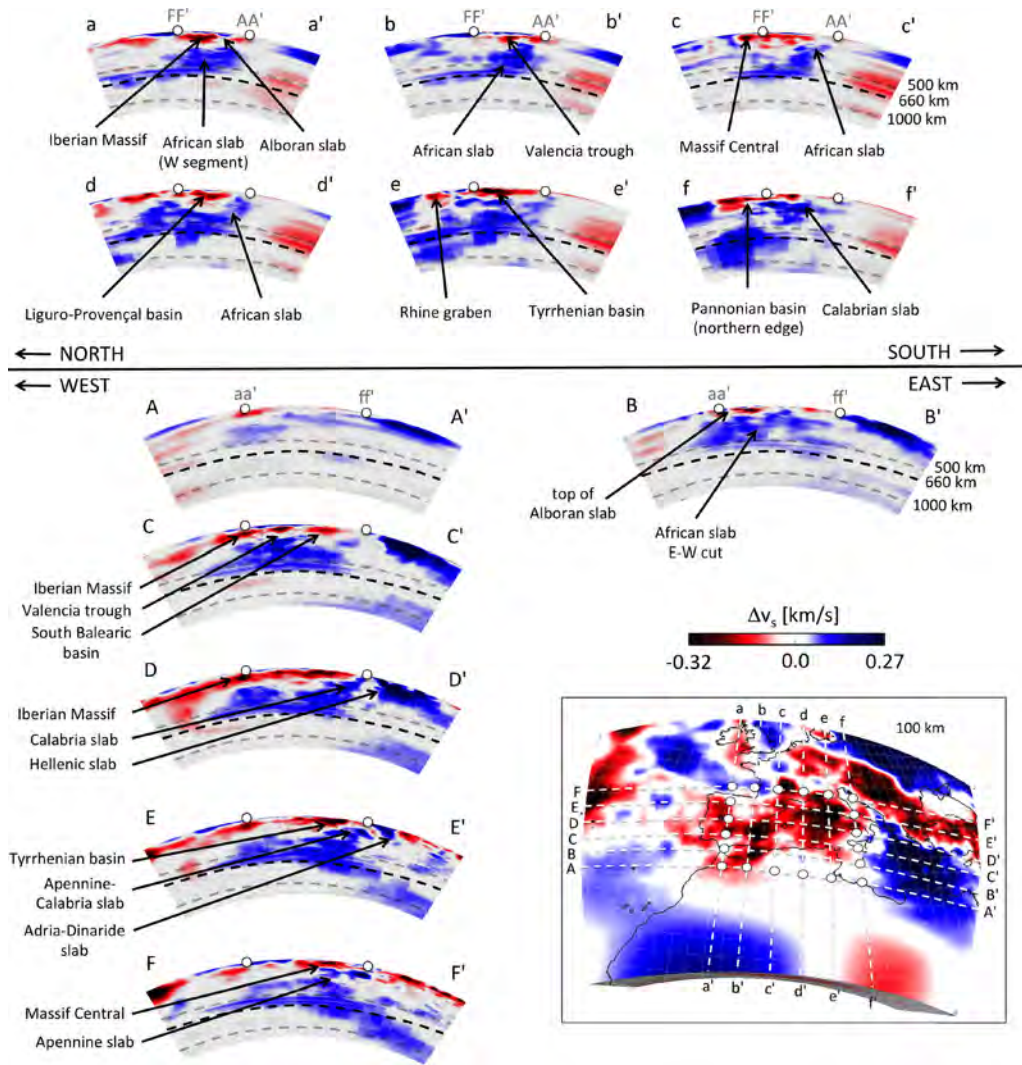


**Fig. 8.** Vertical slices through the absolute variations of isotropic S velocity from 50–1200 km depth. N-S oriented slices are shown in the top rows, and E-W oriented slices are shown below. Dashed lines are plotted for orientation at 500, 660 and 1000 km depth. The location of the profiles is indicated in the inset which shows S velocity variations at 100 km depth. White dots in the inset correspond to white dots in the vertical slices. Variations in absolute velocities are visually slightly enhanced at greater depth compared to relative anomalies due to background velocities increasing with depth.

### 7.1.2. The Alboran–African slab system

The Mediterranean subduction system is visible in the uppermost mantle and transition zone in the form of high-velocity anomalies with  $v_s$  perturbations reaching  $\sim 13\%$ .

The Alboran slab appears around 60 km in Fig. 9 as a curved feature following the geometry of the Gibraltar arc. It continues as separate entity to depths of  $\sim 200$  km, where it starts to interfere with a pronounced E-W trending high-velocity feature that may be interpreted as the African slab. Not previously imaged in similar detail, the African slab between 250–300 km depth appears to be composed of two segments that are slightly offset in NW direction. These are indicated by dotted lines in the enlarged regions of the 250 km and 300 km depth slices of Fig. 9. The segmentation ceases to be visible around 350 km depth and below. Unlike the Alboran slab, the African slab segments are confined to depths below 150 km, possibly indicating slab detachment. In the context of recent tectonic reconstructions (Faccenna et al., 2014), the high-velocity segments beneath Algeria might be remnants of the slab that caused the opening of the Liguro–Provençal basin by roll-back and subsequent back-arc extension.

The vertical structure of the Alboran–African slab system is shown in the N-S oriented cross-sections of Fig. 8 (profiles aa', bb', cc' and dd'). Throughout the upper mantle, the African slab

dips northward before merging into or continuing as a broad high-velocity anomaly underlying central and western Europe at depths of  $\sim 660$  km. Within the anomaly, best visible in the 700 km depth slice of Fig. 9, individual slabs cannot be distinguished.

In addition to the African–Alboran system, all previously identified slabs are present in our model. These include the Alpine, Apennine–Calabria, Adria–Dinaride, and Hellenic slabs. Their respective morphology is consistent with previous studies (e.g. Piromallo and Morelli, 2003; Villaseñor et al., 2003; Koulakov et al., 2009; Zhu et al., 2015).

### 7.2. Comparison with previous tomographic models

Numerous models comprising the western Mediterranean have been constructed in recent years using a variety of techniques ranging from linearised traveltimes tomography with the ray approximation to nonlinear inversions based on numerical wave propagation and adjoint techniques. Differences between models result from differences in methods, data and regularisation. Since a comparison of all models is beyond the scope of this study, we focus on few recently published models constructed with distinct methods and data sets. Our goal is to highlight similarities and the origin of possible differences, acknowledging that subjective



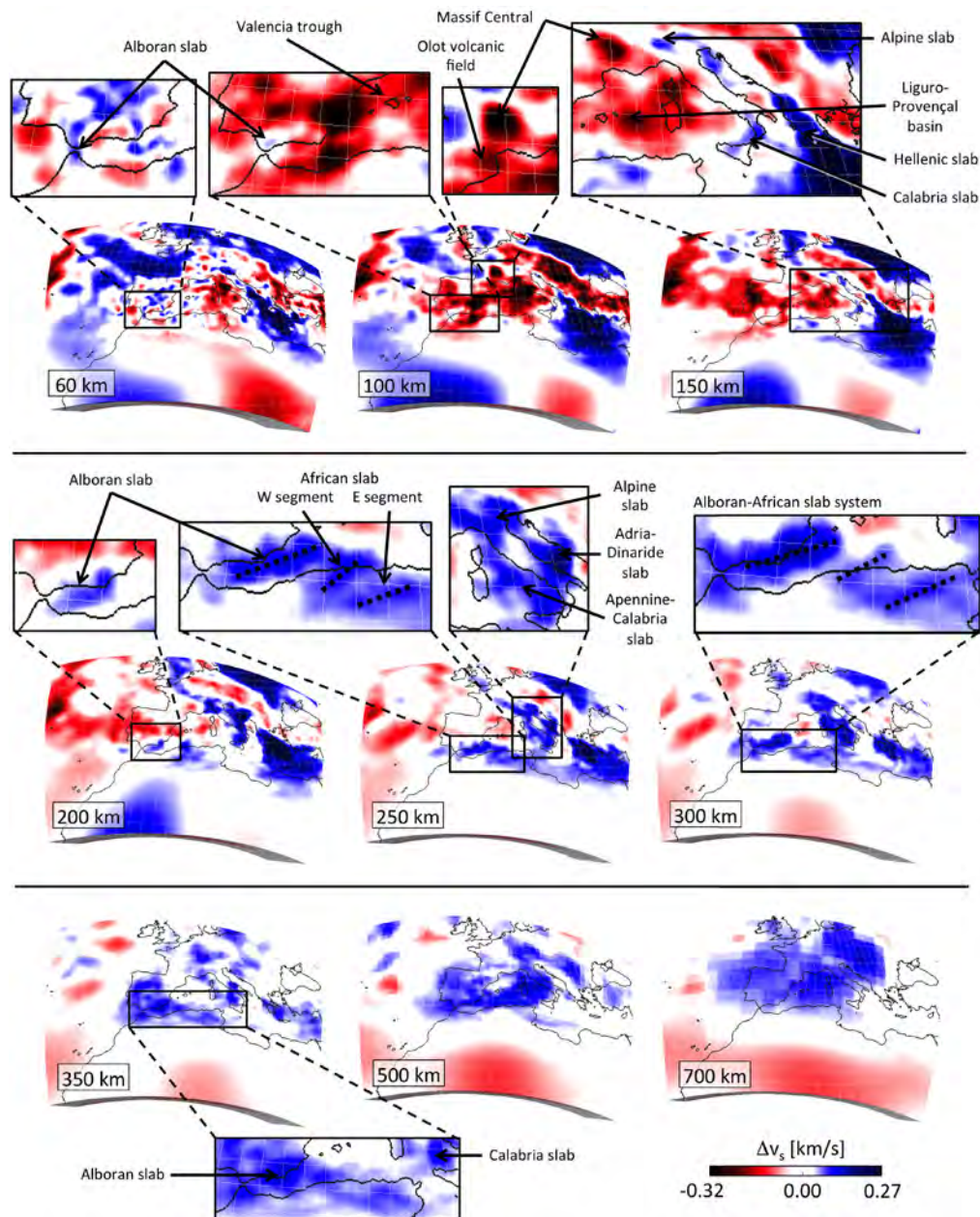


**Fig. 9.** Horizontal slices through the absolute variations of isotropic S velocity from 60–700 km depth. Features mentioned in the text are labelled. Dotted lines in the enlarged panels of the 250 km and 300 km slices mark possible segments of the Alboran–African slab system.

components of tomographic inversion and the common absence of quantitative resolution analyses often permit only qualitative statements.

The P-velocity models of Piromallo and Morelli (2003), Villaseñor et al. (2003) and Koulakov et al. (2009) are based on body wave traveltime measurements made at the International Seismological Centre (ISC). While IberArray was not yet available, the ability to use a large number of north African earthquakes in a computationally less expensive ray tomography, compensated the small number of stations to some extent. Within the upper ~200 km, there is limited similarity between the P-wave models and our model, especially beneath the Mediterranean Sea and northern Africa. Two factors contribute to this observation: (i) Full-waveform inversion and body wave traveltime tomography have different resolution at shallow depth. The vertical smearing in body wave tomography is compensated in full-waveform inversion by the natural incorporation of surface waves. (ii) P and S velocity

respond differently to variations in temperature and composition. The geometry of P and S velocity heterogeneities is not directly comparable unless compositional effects can be excluded. Below ~200 km depth, similarity increases, and all models are dominated by the higher than average velocities of the Mediterranean subduction system. Around 600 km depth, all models show slabs merging into a broad high-velocity structure, though notable differences exist beneath the western Mediterranean. These are most likely caused by differences in coverage before and after the installation of IberArray and other temporary networks.

Palomeras et al. (2014) constructed their model from fundamental-mode Rayleigh waves of teleseismic events in the period range 20–167 s. Their station coverage in the western Mediterranean is nearly identical to the one used in our study. Within the upper 40 km both models reveal a distinct low-velocity anomaly beneath the Strait of Gibraltar, as well as a high-velocity anomaly beneath the Iberian Massif. Below the crust, the high velocities of

the Alboran slab become the dominant feature, though it appears simplified to a nearly circular feature in the model of Palomeras et al. (2014). The approximately E-W trending Alboran slab around 200–300 km depth, featured in the full-waveform and body wave models, is not present in the surface wave model. These discrepancies may result from the absence of body waves that would contribute more lateral resolution, and the limitation to the fundamental mode with limited vertical resolution.

From a methodological perspective, the full-waveform model of Zhu et al. (2015) is most similar to ours. Technical differences in the model construction are limited to details in the numerical mesh, and the definition of waveform misfits. Consequently, both models are similar in regions where data coverage and bandwidth are comparable, that is in central and eastern Europe. A quantitative comparison is difficult because a resolution analysis from which a distribution of resolution lengths could be inferred is not included in the work of Zhu et al. (2015). A point-spread function for eastern Europe suggests horizontal resolution of  $\sim 100$  km. Zhu et al. (2015) included only few stations in the western Mediterranean and set the minimum surface wave period to 25 s, that is around twice the minimum period of 12 s used for our model. This may explain why the African and Alboran slabs are not visible in their tomography.

The main conclusion of this brief comparison is that models are qualitatively similar in regions where spatial and frequency coverage are comparable. Since we incorporate both body and surface waves, our model most closely resembles body wave traveltime tomographies below  $\sim 200$  km depth, and surface wave tomographies above  $\sim 200$  km depth. Remaining differences that cannot be explained by differential resolution are likely to result from inconsistent treatment of the crust, errors in the forward modelling, the treatment of data errors, and differences in regularisation.

## 8. Conclusions

We present a full-waveform tomographic model of the western Mediterranean crust and mantle that is intended to improve our understanding of the regional geodynamic evolution. Using spectral-element simulations of seismic wave propagation combined with adjoint techniques, we invert complete three-component recordings from permanent and temporary networks, including IberArray, the PICASSO experiments, as well as smaller arrays operated by the universities of Münster and Bristol. The natural incorporation of body and multi-mode surface waves in the period range from 12–150 s allows us to jointly resolve crustal and mantle structure. In addition to resolving shallow basins together with deep slabs in one model, this approach minimises contamination of mantle structure by unknown crustal structure, and vice versa.

Our major findings in terms of Earth structure are the following: (i) In addition to the well-studied Alboran slab (e.g. Bezada et al., 2013; Bonnin et al., 2014; Palomeras et al., 2014), an E-W trending high-velocity anomaly is visible around 200–300 km depth beneath the Algerian coast. This African slab is detached from the surface and broken into two segments. It may be interpreted as the slab that caused the opening of the Liguro-Provençal basin through successive roll-back between 35–15 Ma. (ii) No mantle plumes can be detected beneath the European Cenozoic rift system, including the Massif Central and the Eifel hotspot. Previous plume sightings in pure body wave tomography may be an artefact of vertical smearing in the upper mantle (e.g. Granet et al., 1995; Goes et al., 1999; Ritter et al., 2001). (iii) Surface waves with periods below  $\sim 20$  s demand radial anisotropy in the crust. Allowing for crustal anisotropy eliminates the need for strong anisotropy below  $\sim 100$  km depth, as found, for instance, in PREM (Dziewoński and Anderson, 1981).

## Acknowledgements

The authors would like to thank Hans-Peter Bunge, Laura Cobden, Jordi Díaz, Rob Govers, Alan Levander, Cesar Ranero and Martin Schimmel for discussions and comments that helped us to improve the manuscript. We gratefully acknowledge support by the Swiss National Supercomputing Centre (CSCS) in the form of CHRONOS project ch1 and PASC project GeoScale. Furthermore, we thank Lion Krischer for the development of LASIF and the making of Fig. 2. Andreas Fichtner would like to thank his colleagues at ICTJA Barcelona for their kind hospitality and the numerous discussions that helped to improve this manuscript. A digital version of the tomographic model presented in this paper is freely available from the authors upon request.

## References

- Backus, G.E., 1962. Long-wave elastic anisotropy produced by horizontal layering. *J. Geophys. Res.* 67, 4427–4440.
- Backus, G.E., Gilbert, F., 1968. The resolving power of gross Earth data. *Geophys. J. R. Astron. Soc.* 16, 169–205.
- Bezada, M.J., Humphreys, E.D., Toomey, D.R., Harnafi, M., Dávila, J.M., Gallart, J., 2013. Evidence for slab rollback in westernmost Mediterranean from improved upper mantle imaging. *Earth Planet. Sci. Lett.* 368, 51–60.
- Bolt, B.A., 1991. The precision of density estimation deep in the Earth. *Q. J. R. Astron. Soc.* 32, 367–388.
- Bonnin, M., Nolet, G., Villaseñor, A., Gallart, J., Thomas, C., 2014. Multiple-frequency tomography of the upper mantle beneath the African/Iberian collision zone. *Geophys. J. Int.* 198, 1458–1473.
- Capdeville, Y., Guillot, L., Marigo, J.J., 2010. 2-D nonperiodic homogenization to upscale elastic media for P-SV waves. *Geophys. J. Int.* 182, 903–922.
- Cara, M., Nercessian, A., Nolet, G., 1980. New inferences from higher mode data in western Europe and northern Eurasia. *Geophys. J. R. Astron. Soc.* 61, 459–478.
- Chang, S.J., van der Lee, S., Flanagan, M.P., Bedle, H., Marone, F., Matzel, E.M., Pasyanos, M.E., Rodgers, A.J., Romanowicz, B., Schmid, C., 2010. Joint inversion for three-dimensional S velocity mantle structure along the Tethyan margin. *J. Geophys. Res.* 115. <http://dx.doi.org/10.1029/2009JB007204>.
- Chen, P., Zhao, L., Jordan, T.H., 2007. Full 3D tomography for the crustal structure of the Los Angeles region. *Bull. Seismol. Soc. Am.* 97, 1094–1120.
- Dewey, J.F., 1988. Extensional collapse of orogens. *Tectonics* 7, 1123–1139.
- Díaz, J., Villaseñor, A., Gallart, J., Morales, J., Pazos, A., Códoba, D., Pulgar, J., García-Lobón, J.L., Harnafi, M., Topolberia Seismic Working Group, 2009. The IBERAR-RAY broadband seismic network: a new tool to investigate the deep structure beneath Iberia. *ORFEUS Newlett.* 8, 1–6.
- Durek, J.J., Ekström, G., 1996. A radial model of anelasticity consistent with long-period surface wave attenuation. *Bull. Seismol. Soc. Am.* 86, 144–158.
- Dziewoński, A.M., Anderson, D.L., 1981. Preliminary reference Earth model. *Phys. Earth Planet. Inter.* 25, 297–356.
- Faccenna, C., Becker, T.W., Auer, L., Billi, A., Boschi, L., Brun, J.P., Capitanio, F.A., Funiello, F., Horvath, F., Jolivet, L., Piromallo, C., Royden, L.H., Rossetti, F., Serpelloni, E., 2014. Mantle dynamics in the Mediterranean. *Rev. Geophys.* 52, 283–332.
- Faccenna, C., Piromallo, C., Cespo-Blanc, A., Jolivet, L., Rossetti, F., 2004. Lateral slab deformation and the origin of the western Mediterranean arc. *Tectonics* 23. <http://dx.doi.org/10.1029/2002TC001488>.
- Ferreira, A.M.G., Woodhouse, J.H., Visser, K., Trampert, J., 2010. On the robustness of global radially anisotropic surface wave tomography. *J. Geophys. Res.* 115. <http://dx.doi.org/10.1029/2009JB006716>.
- Fichtner, A., Bunge, H.P., Igel, H., 2006. The adjoint method in seismology – I. Theory. *Phys. Earth Planet. Inter.* 157, 86–104.
- Fichtner, A., Kennett, B.L.N., Igel, H., Bunge, H.P., 2008. Theoretical background for continental- and global-scale full-waveform inversion in the time-frequency domain. *Geophys. J. Int.* 175, 665–685.
- Fichtner, A., Kennett, B.L.N., Trampert, J., 2012. Separating intrinsic and apparent anisotropy. *Phys. Earth Planet. Inter.* 219, 11–20.
- Fichtner, A., Saygin, E., Taymaz, T., Cupillard, P., Capdeville, Y., Trampert, J., 2013a. The deep structure of the North Anatolian Fault Zone. *Earth Planet. Sci. Lett.* 373, 109–117.
- Fichtner, A., Trampert, J., 2011. Hessian kernels of seismic data functionals based upon adjoint techniques. *Geophys. J. Int.* 185, 775–798.
- Fichtner, A., Trampert, J., Cupillard, P., Saygin, E., Taymaz, T., Capdeville, Y., Villaseñor, A., 2013b. Multi-scale full waveform inversion. *Geophys. J. Int.* 194, 534–556.
- Fichtner, A., van Leeuwen, T., 2015. Resolution analysis by random probing. *J. Geophys. Res.*, Solid Earth 120. <http://dx.doi.org/10.1002/2015JB012106>.
- Goes, S., Spakman, W., Bijwaard, H., 1999. A lower mantle source for central European volcanism. *Science* 286, 1928–1931.
- Gokhberg, A., Fichtner, A., in press. Full-waveform inversion on heterogeneous HPC systems. *Comput. Geosci.*

- Granet, M., Wilson, M., Achauer, U., 1995. Imaging a mantle plume beneath the French Massif Central. *Earth Planet. Sci. Lett.* 136, 281–296.
- Herrmann, R.B., Benz, H., Ammon, C.J., 2011. Monitoring the earthquake source process in North America. *Bull. Seismol. Soc. Am.* 101, 2609–2625.
- Kennett, B.L.N., Engdahl, E.R., 1991. Traveltimes for global earthquake location and phase identification. *Geophys. J. Int.* 105, 429–465.
- Koulakov, I., Kaban, M.K., Tesauero, M., Cloetingh, S., 2009. P- and S-velocity anomalies in the upper mantle beneath Europe from tomographic inversion of ISC data. *Geophys. J. Int.* 179, 345–366.
- Krischer, L., Fichtner, A., Zukauskaitė, S., Igel, H., 2015. Large-scale seismic inversion framework. *Seismol. Res. Lett.* 86, 1198–1207. <http://dx.doi.org/10.1785/0220140248>.
- Lailly, P., 1983. The seismic inverse problem as a sequence of before stack migrations. In: Bednar, J., Redner, R., Robinson, E., Weglein, A. (Eds.), *Conference on Inverse Scattering: Theory and Application*. Soc. Industr. Appl. Math., Philadelphia, PA.
- Lévéque, J.J., Rivera, L., Wittlinger, G., 1993. On the use of the checkerboard test to assess the resolution of tomographic inversions. *Geophys. J. Int.* 115, 313–318.
- Lonergan, L., White, N., 1997. Origin of the Betic–Rif mountain belt. *Tectonics* 16, 504–522.
- Molnar, P., Houseman, G.A., 2004. The effects of buoyant crust on the gravitational instability of thickened mantle lithosphere at zones of intracontinental convergence. *Geophys. J. Int.* 158, 1134–1150.
- Nolet, G., 1977. The upper mantle under Western Europe inferred from the dispersion of Rayleigh modes. *J. Geophys.* 43, 265–286.
- Palomeras, I., Thurner, S., Levander, A., Liu, K., Nor, A.V., Carbonell, R., Harnafi, M., 2014. Finite-frequency Rayleigh wave tomography of the western Mediterranean: mapping its lithosphere structure. *Geochem. Geophys. Geosyst.* 15. <http://dx.doi.org/10.1002/2013GC004861>.
- Piromallo, C., Morelli, A., 2003. P wave tomography of the mantle under the Alpine–Mediterranean area. *J. Geophys. Res.* 108, 1–23.
- Platt, J.P., Allerton, S., Kirker, A., Mandeville, C., Mayfield, A., Platzmann, E.S., Rimi, A., 2003. The ultimate arc: differential displacement, oroclinal bending, and vertical axis rotation in the external Betic–Rif arc. *Tectonics* 22. <http://dx.doi.org/10.1029/2001TC001321>.
- Rickers, F., Fichtner, A., Trampert, J., 2013. The Iceland – Jan Mayen plume system and its impact on mantle dynamics in the North Atlantic region: evidence from full-waveform inversion. *Earth Planet. Sci. Lett.* 367, 39–51.
- Ritter, J.R.R., Jordan, M., Christensen, U.R., Achauer, U., 2001. A mantle plume below the Eifel volcanic fields, Germany. *Earth Planet. Sci. Lett.* 186, 7–14.
- Spakman, W., van der Lee, S., van der Hilst, R., 1993. Travel-time tomography of the European–Mediterranean mantle down to 1400 km. *Phys. Earth Planet. Inter.* 79, 3–74.
- Spakman, W., Wortel, M.J.R., 2004. A tomographic view of western Mediterranean geodynamics. In: *The TRANSMED Atlas – The Mediterranean Region from Crust to Mantle*. Springer, Berlin, Heidelberg, pp. 31–52.
- Tape, C., Liu, Q., Maggi, A., Tromp, J., 2010. Seismic tomography of the southern California crust based upon spectral-element and adjoint methods. *Geophys. J. Int.* 180, 433–462.
- Tarantola, A., 1984. Inversion of seismic reflection data in the acoustic approximation. *Geophysics* 49, 1259–1266.
- Tromp, J., Tape, C., Liu, Q., 2005. Seismic tomography, adjoint methods, time reversal and banana-doughnut kernels. *Geophys. J. Int.* 160, 195–216.
- Vergés, J., Fernández, M., 2012. Tethys–Atlantic interaction along the Iberia–Africa plate boundary: the Betic–Rif orogenic system. *Tectonophysics* 579, 144–172.
- Villaseñor, A., Ritzwoller, M.H., Levshin, A.L., Barmin, M.P., Engdahl, E.R., Spakman, W., Trampert, J., 2001. Shear velocity structure of central Eurasia from inversion of surface wave velocities. *Phys. Earth Planet. Inter.* 123, 169–184.
- Villaseñor, A., Spakman, W., Engdahl, E.R., 2003. Influence of regional travel times in global tomographic models. *EGS-AGU-EUG Joint Assembly, Research Abstract, EAE03-A-08614*.
- Yanovskaya, T.B., 1997. Resolution estimation in the problems of seismic ray tomography. *Izv. Phys. Solid Earth* 33, 76–80.
- Zhu, H., Bozdag, E., Tromp, J., 2015. Seismic structure of the European upper mantle based on adjoint tomography. *Geophys. J. Int.* 201, 18–52.